J. Fluid Mech. (1988), *vol.* 189, *pp.* 367–395
Printed in Great Britain

Instability of swirl in low-Prandtl-number thermal convection

By JOSEP M. MASSAGUER AND ISABEL MERCADER
E.T.S.E. Camins, Canals i Ports and Facultat d'Informatica, Universitat Politecnica de Catalunya, Jorge Girona 31, Barcelona 08034, Spain

(Received 13 June 1985 and in revised form 22 September 1987)

In the present paper we examine low-Prandtl-number thermal convection using a highly truncated modal approach. For the horizontal structure we assume a hexagonal planform as in Toomre Gough & Spiegel (1977) but including a vertical vorticity mode. The system develops a non-zero vertical vorticity component through a finite-amplitude instability. Following this, the system displays a Hopf bifurcation giving rise to periodic oscillations. The mechanism for this instability is associated with the growth of swirl in the azimuthal direction. We have found three different types of periodic solutions, possibly associated with subharmonic bifurcations, and their structure has been examined.

A large part of the present work is devoted to exploring the cases of mercury and liquid helium – or air – as the best-known examples of low and intermediate-Prandtl-number fluids. Results for mercury are quite satisfactory as far as frequencies and fluxes are concerned and they show reasonable agreement with experimental measurements at mildly supercritical Rayleigh values. On the other hand, for liquid helium or air agreement is poor.

1. Introduction

The aim of this paper is to examine some aspects of the transition to time-dependent flow in low-Prandtl-number thermal convection. Interest in the subject comes mostly from astrophysics and geophysics, where very low Prandtl-number values can be found, though practical applications for liquid metals and crystal growth have recently proved to be a new source of interest. Recent experiments in liquid helium and mercury have shown low-Prandtl-number thermal convection to provide a puzzling example of transition to chaos, with a rich bifurcation pattern which is only partly understood (see Behringer & Ahlers 1982; Walden 1983; Fauve *et al.* 1984*a*, *b* and references therein). A first draft of this pattern has been drawn by Busse and Clever by making a linear stability analysis of straight rolls in an infinite layer – see Busse (1978) and references therein – and the theoretical results are well in agreement with numerical experiments (Lipps 1976; McLaughlin & Orzag 1982; Sulem, Sulem & Thual 1985). They show straight rolls being destabilized at a Rayleigh number of $R \approx 1900$ by an instability of an oscillatory type, resulting in a wave-like distortion that is propagated along the roll with frequencies within the range of the thermal diffusion time.

However, from some laboratory experiments, we may seriously question whether a linear stability analysis of straight rolls can explain the pattern of convection in mildly supercritical regimes. The answer is not clear and the present paper is a quest in this direction. If the container is rectangular and the aspect ratio is large the

answer seems to be in the affirmative (Fauve *et al.* 1984*a*). Discrepancies have been found mostly for small- or intermediate-aspect-ratio boxes, where the geometry is expected to force significant departures from two-dimensional geometry, but they have even been found in some experiments where the aspect ratio is large enough for infinite-layer behaviour to be expected. The most relevant experiments in this respect have been conducted by Ahlers & Behringer (1978) and Behringer & Ahlers (1982) in fluids of intermediate-Prandtl-number values confined in large-aspect-ratio cylindrical boxes. The authors could not even find any steady state at Rayleigh numbers above the critical value.

A second set of experiments that are difficult to reconcile with linear theory has been conducted by Krishnamurti (1973). She explored convection in mercury by using a large-aspect-ratio rectangular box and observed the transition to time dependence at a Rayleigh number of $R \approx 2400$, higher than the value $R \approx 1900$ predicted for the oscillatory instability. In addition, the frequencies measured were found to be much smaller than expected. To be precise, the frequencies predicated for the oscillatory instability scale with the thermal diffusion time, while those that she measured scaled with the viscous diffusion time, the ratio between both frequencies being comparable with the value of the Prandtl number.

Discrepancies between theory and Krishnamurti's experiments in mercury could be understood if it is assumed that the amplitudes for the oscillations at the onset of instability were below the instrumental threshold and increased with an increasing Rayleigh number, frequencies decreasing monotically. However one must then explain why the first measured oscillations display frequencies in the range of viscous timescale. In our opinion this change from thermal to viscous timescales reflects a new balance in the master equations and, associated with it, a new instability not shown by straight rolls.

Our purpose is to examine the linear and nonlinear stability of an non-straight structure. The most important contributions in this direction have been made by using the so-called amplitude equations introduced by Newell & Whitehead (1969) and significantly improved by Siggia & Zippelius (1981) by the inclusion of some contribution from the vertical vorticity component. With this contribution they reproduce with reasonable accuracy every instability described by Clever & Busse, (1974), but their vorticity equation only includes what we have called elsewhere *shape instabilities* (Massaguer & Mercader 1984, see also §2.2 below). These are instabilities that change the shape of the primary flow and, as a distinguishing feature, they can all grow from a straight roll. Other sources of instability may exist if the primary flow shows some finite curvature, as is the case in bent rolls and toroidal flows.

Two examples of such flows can be found in the literature: hexagonal planforms (Toomre, Gough & Spiegel 1977, 1982) and cylindrical axisymmetrical flows (Jones, Moore & Weiss 1976), and we have chosen the former for the present paper as it can easily be extended, for future work, with the inclusion of more horizontal modes. The choice of this modal approach for a low-Prandtl-number fluid has been examined with care as significant differences between axisymmetrical cylindrical flows and hexagonal planforms have been reported by the latter authors, mostly concerning the existence of inertial solutions – what they called fly-wheels. However, differences between convection in the two-dimensional axisymmetrical cylinders and hexagonal planforms have been reported for primary flows with Reynolds numbers larger than one, a regime that will be shown to make them both unstable. Thus, our choice has been dictated by reasons of simplicity.

We shall also concentrate on instabilities with respect to linear and nonlinear perturbations preserving the geometry of the primary flow and we shall avoid what we have called above 'shape instabilities'. This might seem to be inconsistent with the linear stability analysis carried out by Jones & Moore (1979) for an axisymmetrical flow, as they showed this flow to be unstable with respect to non-axisymmetrical perturbations. First, the reader should be forewarned that we do not expect a hexagon to remain a hexagon forever. All we attempt is to develop intuition about some nonlinear processes without being forced to do fully three-dimensional computations. Secondly, a linear stability analysis does not decide which instability sets in first or which grows fastest – for instance, a finite-amplitude instability might be present. Finally, the reader should be aware of the linear analysis of axisymmetrical flows not being completed, because Jones & Moore overlooked the possibility of an axisymmetrical flow with a non-zero vertical vorticity component – taking $m = 0$ in their equation (16) implies $\omega_z = 0$ – and this is the case analogous to the one examined here. We shall include in our model a vertical vorticity component, but still retain the hexagonal geometry. As a result, the flow in every cell will show an azimuthal velocity component but will still display hexagonal symmetry. We can imagine a vortex ring with swirl distributed horizontally in such a way that the mean angular momentum is zero.

This paper is, in a sense, an extension of the one-mode cellular expansion of Toomre *et al.* (1977) with the addition of a new field – the vertical vorticity component. Such an expansion has been used previously to explore thermal convection in a rotating layer by Baker & Spiegel (1975) and magnetoconvection by Van der Borght (1976) and Murphy & Lopez (1985, and references therein). We report here on an instability present in low-Prandtl-number thermal convection. Its general nature is discussed in §2, where a highly truncated model displaying this instability is introduced. The numerical analysis is carried out in §3. A steady family of solutions bifurcating from the old one is examined in §4 and its stability properties are considered. In §5 the modal equations are time evolved and some periodic solutions examined. Finally, in §6, some conclusions concerning the physical relevance of the model are discussed.

2. Mathematical formulation of the problem

Thermal convection will be studied in a plane-parallel domain, horizontally periodic, bounded by two horizontal plates and filled with a Boussinesq fluid. The problem will be specified by two parameters: Rayleigh number R, and Prandtl number σ, both defined in the usual way, the former being a measure of the external forcing and the latter a ratio of two timescales: thermal and viscous diffusion times. Two more parameters specifying the horizontal structure will be introduced in §2.3.

2.1. *The exact equations*

In a Boussinesq fluid the velocity field $\boldsymbol{v}$ is assumed to be solenoidal:

$$\boldsymbol{\nabla} \cdot \boldsymbol{v} = 0. \tag{2.1}$$

If, in addition, the mean velocity along a direction $\boldsymbol{k}$ is zero, then $\boldsymbol{v}$ can be written as a sum of a poloidal plus a toroidal component

$$\boldsymbol{v} = \boldsymbol{\nabla} \times \boldsymbol{\nabla} \times (\phi \boldsymbol{k}) + \boldsymbol{\nabla} \times (\psi \boldsymbol{k}), \tag{2.2a}$$

where $\boldsymbol{k}$ is unit vector pointing upwards along the positive z-axis and ϕ and ψ are two scalar fields related to the vertical components of the velocity and vorticity by the expressions

$$v_z = -\nabla_1^2 \phi, \tag{2.2b}$$

$$\omega_z = -\nabla_1^2 \psi, \tag{2.2c}$$

where $\boldsymbol{\omega} = \boldsymbol{\nabla} \times \boldsymbol{v}$ is the vorticity vector, $\boldsymbol{\nabla}_1 = (\partial_x, \partial_y, 0)$ the horizontal projection of the grad vector, and ∇_1^2 the horizontal Laplacian.

We can now write the Navier–Stokes equation for a Boussinesq fluid with no mean motion in terms of ϕ and ψ. By projecting the equation by the curl $(\boldsymbol{\nabla} \times\ )$ and the double curl $(\boldsymbol{\nabla} \times \boldsymbol{\nabla} \times\ )$ operators, the vertical components of both projections can be written as

$$(\sigma^{-1} \partial_t - \nabla^2) \nabla^2 v_z = -R \nabla_1^2 T + \sigma^{-1} [\boldsymbol{\nabla} \times \boldsymbol{\nabla} \times (\boldsymbol{v} \cdot \boldsymbol{\nabla} \boldsymbol{v})]_z \tag{2.3}$$

and

$$(\sigma^{-1} \partial_t - \nabla^2) \omega_z = -\sigma^{-1} [\boldsymbol{v} \cdot \boldsymbol{\nabla} \omega_z - \boldsymbol{\omega} \cdot \boldsymbol{\nabla} v_z], \tag{2.4}$$

where T is the temperature field and all magnitudes have been made dimensionless. The units for space, time and temperature have been taken to be the thickness of the layer, the thermal diffusion time, and the temperature difference across the layer respectively. Equations (2.3) and (2.4) are complemented with the heat equation, written in these units as

$$(\partial_t - \nabla^2) T = -\boldsymbol{v} \cdot \boldsymbol{\nabla} T. \tag{2.5}$$

The system formed by (2.2)–(2.5) can be solved for the three scalar fields ϕ, ψ and T provided that appropriate boundary conditions are imposed. We have assumed rigid boundary conditions for the velocity:

$$v_z = \partial_z v_z = \omega_z = 0 \quad \text{at } z = 0, 1, \tag{2.6}$$

and perfectly conducting plates with imposed temperature at top and bottom:

$$T(z = 0) = 1; \quad T(z = 1) = 0. \tag{2.7}$$

For convenience we shall split each scalar field, say T, into its horizontal average $\bar{T}$ and the fluctuation T', where an overbar means horizontal average. We can write

$$T(x, y, z, t) = \bar{T}(z, t) + T'(x, y, z, t), \tag{2.8}$$

with

$$\bar{T}' = 0.$$

Now, from the horizontal average of the continuity equation (2.1), the condition $\boldsymbol{\nabla} \cdot \boldsymbol{\omega} = 0$, and the imposed boundary conditions we obtain

$$\bar{v}_z = \bar{\omega}_z = 0. \tag{2.9}$$

Also, from the average of (2.2) we obtain

$$\bar{\phi} = \bar{\psi} = 0, \tag{2.10}$$

where horizontal periodicity has been assumed.

From previous considerations it can be proved that the horizontal average of (2.3) and (2.4) is identically zero. This is not the case for the heat equation, the horizontal average of which can be written as

$$\partial_t \bar{T} + \partial_z (-\partial_z \bar{T} + \overline{v_z T'}) = 0. \tag{2.11}$$

The average of (2.3) and (2.4) being zero, they themselves provide the fluctuating equations though, for convenience, T in (2.3) is replaced by T'. The equation for T' can be obtained as a difference between (2.5) and (2.11) as

$$(\partial_t - \nabla^2) T' = -\boldsymbol{\nabla} \cdot (\boldsymbol{v}T' - \overline{\boldsymbol{v}T'}) - v_z \partial_z \bar{T}. \tag{2.12}$$

Now, from (2.11) we can introduce Nusselt number N,

$$N = -\partial_z \bar{T} + \overline{v_z T'}, \tag{2.13}$$

as a measurement of the heat flux. The quantity N is constant if the flow is steady. Otherwise, it is convenient to define the top and bottom Nusselt numbers as

$$N_{\mathrm{T}} = -\partial_z \bar{T}(z=1); \quad N_{\mathrm{B}} = -\partial_z \bar{T}(z=0), \tag{2.14}$$

such that in a steady regime $N = N_{\mathrm{T}} = N_{\mathrm{B}}$.

2.2. *On the vorticity equation*

The main difference between the present work and others using similar techniques lies in the vorticity equation, the structure of which deserves some comment. If relationship (2.2) is used, (2.4) can be written explicitly as

$$(\partial_t - \sigma\nabla^2) \nabla_1^2 \psi + \Lambda(\phi, \psi) + \frac{\partial(\nabla_1^2 \psi, \psi)}{\partial(x,y)} = \frac{\partial(\nabla^2 \phi, \nabla_1^2 \phi)}{\partial(x,y)}, \tag{2.15}$$

where

$$\Lambda(\phi, \psi) = \boldsymbol{\nabla}(\partial_z \phi) \cdot \boldsymbol{\nabla}(\nabla_1^2 \psi) - \boldsymbol{\nabla}(\partial_z \psi) \cdot \boldsymbol{\nabla}(\nabla_1^2 \phi) + \nabla^2 \psi \, \partial_z \nabla_1^2 \phi - \nabla^2 \phi \, \partial_z \nabla_1^2 \psi.$$

There are only two circumstances in which the vertical vorticity component can be taken – and has been taken by several authors – to be zero. First, for small amplitudes, for then (2.15) becomes a diffusion equation for ψ. Secondly, if the flow is assumed to be two-dimensional (i.e. dependent on only one horizontal and one vertical component as in the plane or axisymmetrical cases), for then the two Jacobians are zero and the equation becomes linear in ψ, accepting $\psi = 0$ for any ϕ as a particular solution, though other solution may exist.

It can be realized from a standard energy balance (see Appendix) that in (2.15) there are two source terms, the Jacobian on the right-hand side and the term $\Lambda(\phi, \psi)$. As will be shown below, each one of these can be associated with a different family of instabilities. While the Jacobian on the right-hand side acts as an external forcing, resulting in a continuous growth of ψ from the onset of convection, the instability associated with the Λ-term requires a finite value of ϕ.

In order to examine both types of instability, we can take as a primary – unperturbed – flow a two-dimensional field with zero vertical vorticity, say $\{\phi_0, \psi = 0\}$, and $\{\phi', \psi'\}$ as a perturbation field. The linearized version of (2.15) then reads

$$(\partial_t - \sigma\nabla^2) \nabla_1^2 \psi' + \Lambda(\phi_0, \psi') = \frac{\partial(\nabla^2 \phi_0, \nabla_1^2 \phi')}{\partial(x,y)} + \frac{\partial(\nabla^2 \phi', \nabla_1^2 \phi_0)}{\partial(x,y)},$$

where Λ has been defined above. If the primary flow is a straight roll (say $\partial_y \phi = 0$) it has been proved by Busse (1972) that the volume average $\langle \psi' \Lambda(\phi_0, \psi') \rangle$ will be zero and the Λ-term will not make any contribution to the instability – see also (A6) in the Appendix for a similar conclusion. Thus the only source terms are the Jacobians on the right-hand side. Notice that these terms are different from zero only if the perturbation does not preserve the two-dimensional structure of the primary flow.

We have called the instabilities associated with these Jacobians *shape instabilities* for they include most known shape changes – Eckhaus instability is an obvious exception for it is two-dimensional. If the flow is two-dimensional and the geometry is preserved by the perturbations, then (2.15) can be written as

$$(\partial_t - \sigma\nabla^2)\nabla_1^2\psi + A(\phi,\psi) = 0. \tag{2.16}$$

The source term for this equation is different from zero only in those cases where ϕ does not correspond to a straight roll; therefore the flow must show some curvature in order to be destabilized.

In order to explain the physics of this source term we shall consider here the axisymmetrical case and report a more general discussion in the Appendix. In cylindrical coordinates the azimuthal component of the velocity field v_θ is related with the vertical component of the vorticity by the expression $\omega_z = \frac{1}{r}\partial_r(rv_\theta)$. If, instead of (2.16), we now write the azimuthal component of the Navier–Stokes equation,

$$\partial_t v_\theta + \boldsymbol{v}\cdot\nabla v_\theta + \frac{v_r v_\theta}{r} = \sigma\mathscr{L}v_\theta,$$

where $\mathscr{L}v_\theta = \boldsymbol{e}_\theta\nabla^2(v_\theta\boldsymbol{e}_\theta)$ and we take the volume average of the product of this equation times v_θ, followed by a partial integration, we obtain the balance equation

$$\sigma^{-1}\partial_t\langle\tfrac{1}{2}v_\theta^2\rangle + \langle|\nabla(v_\theta\boldsymbol{e}_\theta)|^2\rangle = -\sigma^{-1}\left\langle\frac{v_r v_\theta^2}{r}\right\rangle, \tag{2.17}$$

where, v_r not being either positively or negatively defined, the right-hand side can be positive, acting as a source term for azimuthal velocity component – called the swirl in vorticity dynamics.

The v_θ-equation suggests that we can understand this instability in the following way. In an axisymmetrical flow without swirl (i.e. $v_\theta = 0$) any particle will circle on a vertical plane containing the radial direction. If a parcel of fluid is taken out of this plane then $v_\theta \neq 0$. In a frame of reference rotating around the symmetry axis with angular velocity v_θ/r the parcel will be acted upon by a Coriolis force $2v_\theta v_r/r$ – the reader should be aware that half that force is hinted at in the $\boldsymbol{v}\cdot\nabla v_\theta$ term. For a fixed value of v_θ this force is either a stabilizing or destabilizing one depending on the sign of the radial velocity – i.e. depending on the parcel being in the upper or in the lower half of the layer. Therefore, the Coriolis forces can destabilize the swirl. Such an explanation might raise some doubts about the very nature of the source term in (2.17), for Coriolis forces do no work. Yet, as is well known, the inertial forces as a whole do no net work (see (A 3)) and the term on the right-hand side of (2.17) corresponds to an energy transfer from the radial to azimuthal direction. In that respect, we call the reader's attention to Coles's (1965) description of the Taylor–Couette instability, for it shows the argument inverted: how a radial component v_r can grow from an azimuthal flow.

From (2.17) it is clear that the source term for the instability of swirl is to be zero for a flow symmetrical with respect to a plane at mid-height, for, with v_r changing sign there, the contributions from the upper and lower layers cancel. It is precisely such a lack of asymmetry that explains why some models fail to display such instability. For instance, this seems to be the case in Siggia & Zippelius (1981) – the only source term in their equation (1 *b*) is the Jacobian on the right-hand side of our (2.15). In that case the symmetry was imposed by the bias of the vertical structure of the unperturbed roll.

2.3. *The model equations*

In order to solve the system (2.3), (2.4), (2.11) and (2.12) we shall expand the fluctuating variables on a set of orthogonal functions $\{f_i(x,y)\}$ with amplitude coefficients depending on the variables z and t. If the set of functions is a finite subset of a complete basis the procedure is called the Galerkin method. Its extension to the Boussinesq problem can be found in Gough, Spiegel & Toomre (1975) for those cases with zero vertical vorticity. Inclusion of a vertical vorticity component for a plane geometry was carried out by Baker & Spiegel (1975) in order to study convection in a rotating layer. Our work is based on their model, but we have concentrated on the non-rotating case.

In the present paper we have followed the same path as Toomre *et al.* (1977) and reduced the expansion to only one basis function $f(x,y)$. We are aware of Marcus's (1981) warnings against poor representations of the turbulent spectra, but the results presented in the following sections mostly concern small supercritical Rayleigh values and we are expecting an almost laminar regime. The one-mode expansion chosen for the fields can be written as

$$v_z = f(x,y)\, W(z,t), \tag{2.18a}$$

$$\omega_z = f(x,y)\, \xi(z,t), \tag{2.18b}$$

$$T = \bar{T}(z,t) + f(x,y)\, \theta(z,t), \tag{2.18c}$$

where $f(x,y)$ is taken to be an eigenfunction of the Laplacian operator $\nabla_1^2 f = -a^2 f$. The horizontal velocity components can then be written as

$$v_x = a^{-2}(\partial_x f \partial_z W + \partial_y f \xi),$$

$$v_y = a^{-2}(\partial_y f \partial_z W - \partial_x f \xi).$$

If $f(x,y)$ is to be determined completely, we must impose some boundary conditions and normalize its amplitude. However, for the present purpose $f(x,y)$ can be defined by the three moments $\overline{f} = 0, \overline{f^2} = 1, \overline{f^3} = 2C$. The coupling coefficient C, together with the wavenumber a are parameters we need in order to specify the horizontal structure of the flow. Introduction of (2.18) in (2.3), (2.4) and (2.12) plus horizontal averaging of these equations multiplied previously by $f(x,y)$, gives

$$(\sigma^{-1}\partial_t - \nabla^2)\nabla^2 W = -Ra^2\theta - C\sigma^{-1}(W\partial_z \nabla^2 W + 2\partial_z W \nabla^2 W + 3\xi \partial_z \xi), \tag{2.19a}$$

$$(\sigma^{-1}\partial_t - \nabla^2)\xi = -C\sigma^{-1}(W\partial_z \xi - \xi \partial_z W), \tag{2.19b}$$

$$(\partial_t - \nabla^2)\theta = -W\partial_z \bar{T} - C(2W\partial_z \theta + \theta \partial_z W), \tag{2.19c}$$

$$(\partial_t - \partial_{zz}^2)\bar{T} = -\partial_z(W\theta), \tag{2.19d}$$

where $\nabla^2 = \partial_{zz}^2 - a^2$. In the previous set we have included the averaged equation (2.11). The boundary conditions (2.6) and (2.7) will be written as

$$W = \partial_z W = \xi = 0 \quad (z = 0,1), \tag{2.20}$$

$$\theta = 0 \qquad (z = 0,1), \tag{2.21a}$$

$$\bar{T}(z=0) = 1; \qquad \bar{T}(z=1) = 0. \tag{2.21b}$$

The Nusselt number defined in (2.13) reads

$$N = -\partial_z \bar{T} + W\theta, \tag{2.22}$$

with its top and bottom values defined as in (2.14).

The system (2.19) has been explored numerically in the case of $\xi = 0$ by Toomre *et al.* (1977). Also, Murphy & Lopez (1984), Lopez & Murphy (1984), Mercader (1985), and Mercader & Massaguer (1983) have examined the steady solutions of system (2.19) for the free-boundary case. A first look at time dependence can be found in Massaguer & Mercader (1984) and Murphy & Yannios (1985).

The set of equations (2.19) constitutes our master system throughout the present paper. References to the horizontal structure will not longer be made, meaning that any perturbation of the basic flow will keep its horizontal geometry. Our purpose is to consider system (2.19) as a self-contained dynamic system. It incorporates here the ξ-equation, coupled with the whole system through a quadratic term in ξ: the term $\xi \partial_z \xi$ in (2.19*a*). The steady solutions show a four-fold degeneracy because they present two sets of invariances:

(i) skew-symmetry about the mid-plane for the fluctuating variables while the mean fields remain symmetrical:

$$\{W, \xi, \theta, \partial_z \bar{T}\} \to \{-W, -\xi, -\theta, \partial_z \bar{T}\} \quad \text{for } z \to 1-z;$$

(ii) change in sign for the vertical vorticity, all other variables being unchanged

$$\{W, \xi, \theta, \partial_z \bar{T}\} \to \{W, -\xi, \theta, \partial_z \bar{T}\} \quad \text{for } z \to z.$$

Therefore, each solution found represents a set of four indistinguishable solutions.

3. Stability of $\xi = 0$ solutions

In the small-amplitude limit the system (2.19) breaks down into two uncoupled parts: a linear system for the variables $\{W, \theta, \bar{T}\}$ plus a diffusion equation for ξ. Thus, in the small-amplitude limit any solution is attracted towards $\xi = 0$. These $\xi = 0$ solutions can be taken as zero-order terms for a small-amplitude expansion but, the right-hand side of (2.19*b*) being quadratic, the ξ-equation turns out to be a diffusion equation at each order in powers of the amplitude, and no $\xi \neq 0$ solution can be found. From inspection of (2.19*b*) it is clear that a $\xi \neq 0$ solution is not possible unless W is order one. Therefore a $\xi \neq 0$ solution must grow as a bifurcation from a finite-W solution.

The first step before making a stability analysis is to compute solutions of (2.19) with $\xi = 0$. This system has been studied numerically by Toomre *et al.* (1977) and their solutions have been found to be steady across the whole range of values explored. Therefore we have assumed the primary flow $\{W, \theta, \bar{T}\}$ to be a solution of

$$\nabla^2 \nabla^2 W = Ra^2\, \theta + C\sigma^{-1}(W \partial_z \nabla^2 W + 2\, \partial_z W \nabla^2 W), \tag{3.1a}$$

$$\nabla^2 \theta = W \partial_z \bar{T} + C(2W \partial_z \theta + \theta \partial_z W), \tag{3.1b}$$

$$N = -\partial_z \bar{T} + W\theta, \tag{3.1c}$$

where, the system being steady, we have used the integrated form (2.22) for the heat equation (2.19*d*). N is now a constant and the system has been reduced, as in Toomre

et al. (1977), by eliminating $\partial_z \bar{T}$ and rescaling θ and R by a factor N, with the Nusselt number being computed afterwards from the expression

$$N-1 = \int_0^1 W\,\theta\,\mathrm{d}z.$$

The linear perturbation of the primary flow is very simple, as the coupling between the ξ-equation and the whole system depends on a term that is quadratic in ξ. The linear stability analysis breaks the problem down into two parts in such a way that the stability for ξ can be considered independently of that for other variables. Thus, the stability for ξ keeps the form (2.19*b*), W being there a solution of (3.1) with the same parameters C and a. Equation (2.19*b*) now becomes a linear problem with time-independent coefficients. Assuming an exponential growth rate it can be reduced to an eigenvalue problem. For convenience we have made the following change of variable:

$$\xi(z,t) = h(z)\exp\left[\lambda t + \frac{C}{2\sigma}\int_0^z W\,\mathrm{d}z\right],$$

and (2.19*b*) can be written as

$$\left[\partial_{zz}^2 + \left(\gamma - \frac{\lambda}{\sigma}\right)\right]h = 0, \tag{3.2}$$

with

$$\gamma = \frac{3C}{2\sigma}\partial_z W - \left[a^2 + \left(\frac{CW}{2\sigma}\right)^2\right].$$

The boundary conditions are

$$h = 0 \quad \text{at } z = 0, 1.$$

It is now obvious that the problem is self-adjoint, λ must be real, and the states of marginal stability can be found by solving (3.2) with $\lambda = 0$. If the velocity field is normalized as $W = \epsilon\hat{W}$, with ϵ defined as the maximum value of W, and we take $Re = C\epsilon/\sigma$ as Reynolds number for the primary flow, (3.2) for the marginal state can be written as

$$\partial_{zz}^2 h + \gamma h = 0, \tag{3.3a}$$

with

$$\gamma = -a^{-2} + \tfrac{3}{2}Re\,\partial_z \hat{W} - (\tfrac{1}{2}Re)^2\,\hat{W} \tag{3.3b}$$

and

$$h = 0 \quad \text{at } z = 0, 1.$$

Equation (3.3*a*) is of the Helmholtz type and its properties are well known in the literature. One necessary requirement for a non-trivial solution is that γ be positive somewhere in the $z = 0, 1$ interval, but, by inspection of (3.3*b*) we can conclude that γ is not positive if Re is much larger or smaller than one, and a is order one or smaller. Then, for γ to be positive at some point, Re must be order one.

3.1. *Numerical analysis*

System (3.1) has been solved numerically by using a second-order finite-difference scheme together with a Newton–Raphson iteration technique. A uniformly spaced grid was used with the number of points ranging from 51 to 101. In the range of parameters explored the solutions were found to be smooth enough, and the boundary layers reasonably thick, to solve the equations without using mesh-stretching. We have solved (3.1) for each set of R, C, a and σ values and the W-field obtained has been used to evaluate the coefficients in (3.2). The eigenvalue problem

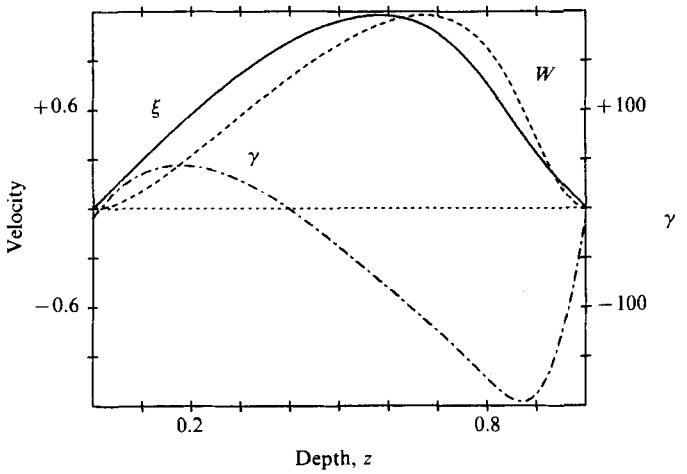

FIGURE 1. Eigenfunction ξ (——) as a function of depth z for the stability of a $\xi = 0$ solution at the bifurcation point $R_T = 3848$, $\sigma = 0.025$, $a = 3.117$ together with the velocity field W (– – –) and the function γ (– · –) defined in (3.2). The amplitude of ξ has been normalized by the maximum value of W to help in comparison. The function γ shows two zeros, as discussed in the text. Both zeros are located in the lower half of the layer ($z < 0.4$).

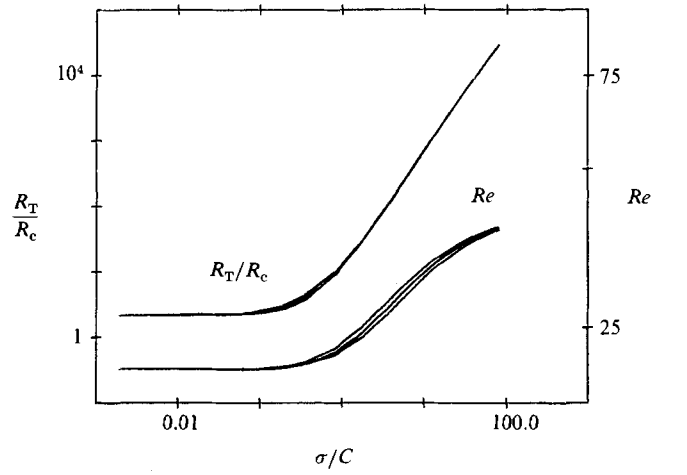

FIGURE 2. Rayleigh number R_T and Reynolds number Re for the bifurcations $\xi = 0$ solutions, plotted as a function of σ/C for $a_c = 3.117$ for three different values of C: 0.2, 0.4, 0.6. Their asymptotic values at small Prandtl-number values are $R = 3650$ and $Re = 20.87$. The bifurcation is almost independent of C for fixed σ/C.

(3.2) was then solved by again using a second-order finite-difference scheme. Finally, the eigenfunction ξ was computed using a standard quadrature formula.

As default values for a and C we have taken $a = 3.117$ and $C = 1/\sqrt{6}$ corresponding, respectively, to the critical wavenumber a_c of the linear problem and the coupling constant for hexagons. In figure 1 we have plotted a W-solution for (3.1) at the bifurcation point $R_T = 3848$, $\sigma = 0.025$ along with the function γ and the eigenfunction ξ. For these boundary conditions the function γ must show at least two

zeros, as shown in the figure, since γ must be positive somewhere on the interval and since the boundary conditions $W = \partial_z W = 0$ imply a negative value for γ at both its ends.

The main concern of this work is the analysis of the asymptotic limit $\sigma \to 0$. In figure 2 we have plotted the Rayleigh R_T and Reynolds Re number against Prandtl number for the state of marginal stability of $\xi = 0$ steady solutions. Results have been plotted for different C-values but we have taken as abscissa the ratio σ/C to show that all results fit on the same curve, with the implication that the C-term in (2.19*c*) – i.e the only one dependent on C but not on C/σ – does not make any significant contribution to this instability. In the small-Prandtl-number limit these curves of marginal stability asymptote to $R = 3650$ and $Re = 20.87$ for the critical wavenumber. The limit is reached near the $\sigma/C = 0.1$ value. Mercury, with $\sigma = 0.025$, fits the limit, but neither air not liquid helium ($\sigma \approx 0.7$) do. The existence of such an asymptotic limit is consistent with the results obtained by Mercader & Massaguer (1983) for free boundary conditions but not with those of Murphy & Lopez (1984), for they propose the asymptotic law $R \sim 10^3 \sigma^{1.5}$. In support of our results we present a small-amplitude analysis as in Malkus & Veronis (1958) or Schlüter, Lortz & Busse (1965) – see also Gough *et al.* (1975). At second order in amplitude they obtain

$$\epsilon = \left[\frac{R - R_c}{R_2}\right]^{\frac{1}{2}},$$

where, in the limit of small σ, $R_2 = R_c Q^2 C^2 \sigma^{-2}$ with Q being a constant dependent on the wavenumber and boundary conditions. Thus, the Reynolds number can be written as

$$Re = \frac{C\epsilon}{\sigma} = Q^{-1}\left[\frac{R}{R_c} - 1\right]^{\frac{1}{2}}. \tag{3.4}$$

In addition, in this limit $W = \hat{W}_0 + Re\,\hat{W}_1 + O(\sigma Re)$ from which $\gamma = \gamma(z; Re, a)$ and γ becomes independent of σ, as can be seen from its definition (3.3*b*). The eigenvalue in (3.3) with fixed a is now the Reynolds number Re. In consequence, the asymptotic limit for Re depends only on the wavenumber. This asymptotic behaviour for Re might be inferred from the results displayed by Murphy & Lopez (1984) in their figure 5, though, strictly speaking, they are not defining a bifurcation. From that result and (3.4) we can conclude that the Rayleigh number for the bifurcation R_T is independent of σ, as found numerically. How the marginal state depends on the wavenumber will be shown in figure 6, but we can we can now state that the minimum value for the Rayleigh number has been found to be at $R_T = 3293$, corresponding to the wavenumber $a = 2.25$ – smaller than the critical one.

4. Nonlinear steady solutions

In the previous section we found the bifurcation to $\xi \neq 0$ to be non-oscillatory. The next logical step is to search for steady solutions to the complete system. Therefore we have solved (2.19) numerically by using the technique outlined at the beginning of §3.1. In figure 3 we have plotted two sets of fields corresponding to the cases with and without vertical vorticity, respectively. We have chosen the values $R = 8000$, $\sigma = 0.025$ and $a = 3.117$ for these solutions. Their Reynolds numbers are, respectively, $Re = 25.90$ and $Re = 44.96$, to be compared with the asymptotic limit

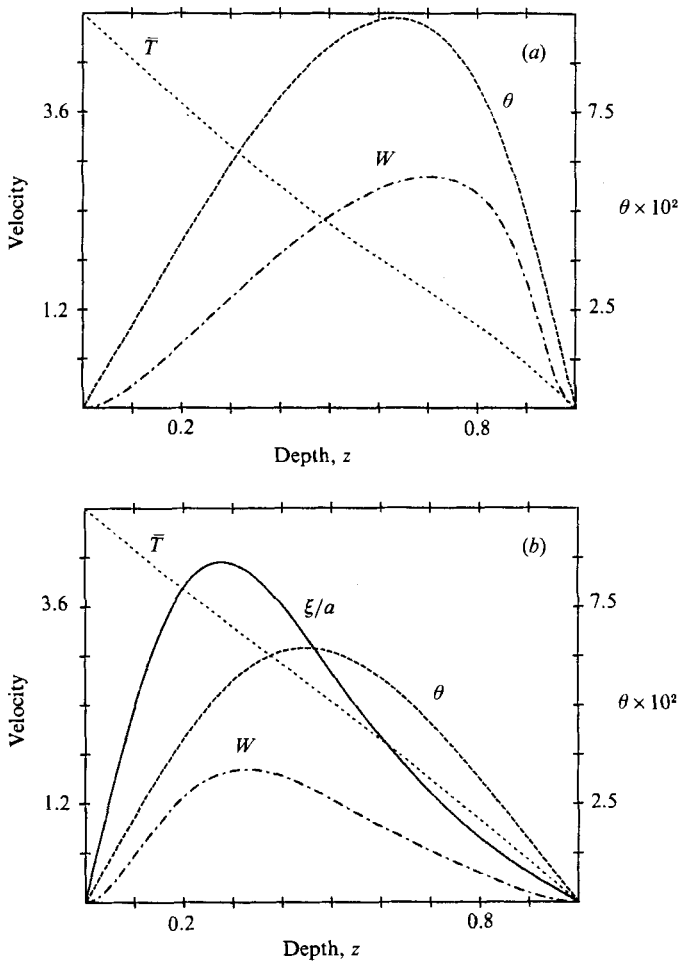

FIGURE 3. Two steady solutions at $R = 8000$, $a = 3.117$, $\sigma = 0.025$ for the cases (*a*) $\xi = 0$ and (*b*) $\xi \neq 0$. They are only slightly nonlinear, as shown by their Nusselt numbers being $N = 1.15$ and $N = 1.04$, respectively. In both cases $\bar{T}$ (.....) is almost linear, but W and θ (– · – lines respectively) have been significantly distorted by the presence of a $\xi \neq 0$ component, as can be seen by comparing (*a*) and (*b*). To compare with W, ξ has been scaled by a factor a – see definition of E_K below.

$Re = 20.87$. The relative contribution of the ξ-component to the flow can be measured by the kinetic-energy fraction

$$q = \frac{a^{-2}\int_0^1 \xi^2\, dz}{2E_K},$$

where

$$E_K = \langle \tfrac{1}{2} v^2 \rangle = \int_0^1 \tfrac{1}{2}\{a^{-2}[(\partial_z W)^2 + \xi^2] + W^2\}\, dz$$

is the total kinetic energy. For the case presented in figure 3(*b*) we have obtained the value $q = 0.72$, showing a very large contribution to the flow by the ξ-mode, which results in a significant distortion of the W- and θ-fields.

In order to describe the bifurcation we have plotted Nusselt number versus Rayleigh number for mercury and liquid helium in figures 4 and 5. In both cases the

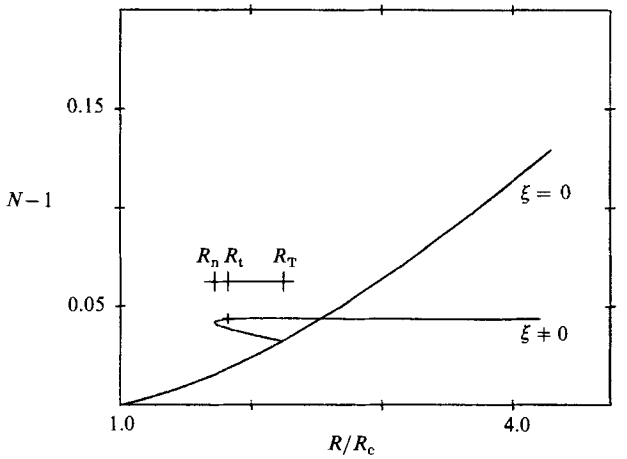

FIGURE 4. Nusselt number N versus Rayleigh R for a set of solutions with $\sigma = 0.025$, $a = 3.117$. Each line is labelled with $\xi = 0$ or $\xi \neq 0$ depending on the type of solution represented. On top of the figure we have displayed the positions of the points R_n, R_t and R_T – see text. For clarity we have plotted a cross on the Hopf bifurcation. The values for these points are $R_n = 2940$, $R_t = 3117$, $R_T = 3848$ and $R_c = 1708$.

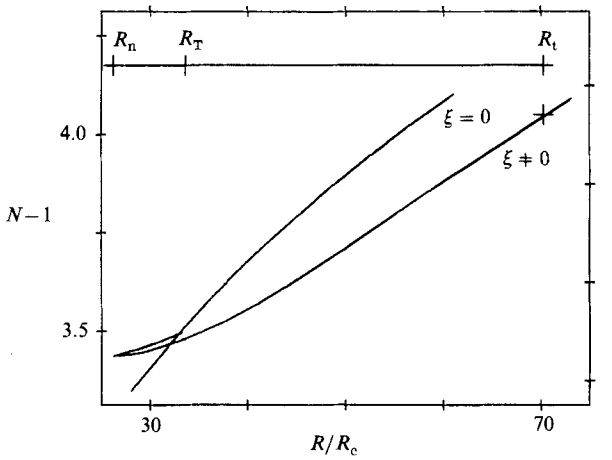

FIGURE 5. As figure 4 but for $\sigma = 0.78$, and now $R_n = 45134$, $R_t = 1.2 \times 10^5$ $R_T = 57377$. It can be observed that the relative positions of R_t and R_T are now inverted and the Hopf bifurcation does not take place on the metastable section of the new branch.

bifurcation at R_T was found to be subcritical, giving rise to a finite-amplitude instability. The points where the instability can be triggered have been labelled R_n – we shall call these points 'nose points'. In both cases the new family of solutions is less efficient in transporting heat than the old one, as can be seen from the Nusselt numbers being smaller almost everywhere. If figures 4 and 5 are compared, it can be seen that the slope of the new branch decreases with σ, with the implication that the difference in heat transport between the $\xi = 0$ and $\xi \neq 0$ solutions is significant for low σ but negligible for intermediate values.

There is an additional point to be remarked on in figures 4 and 5. In both cases the

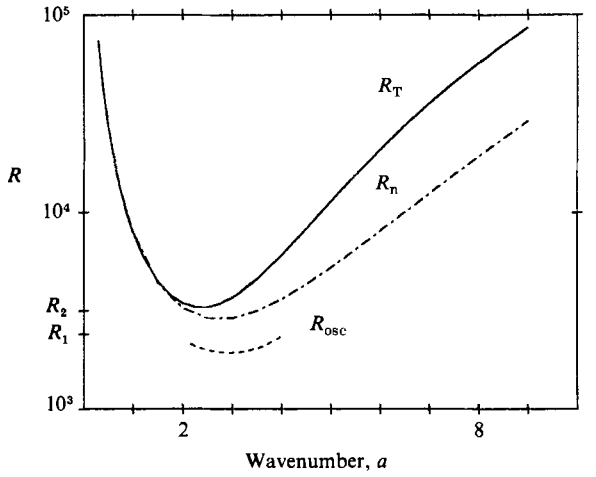

FIGURE 6. Rayleigh numbers R_T and R_n for $\sigma = 0.025$ as a function of the wavenumber a. We have included for comparison the first and second transitions to time dependence reported by Krishnamurti (1973), displayed on the axis as R_1 and R_2, because no information exists about wavenumbers. We have also included Clever & Busse's (1974) results on the oscillatory instability as R_{osc}.

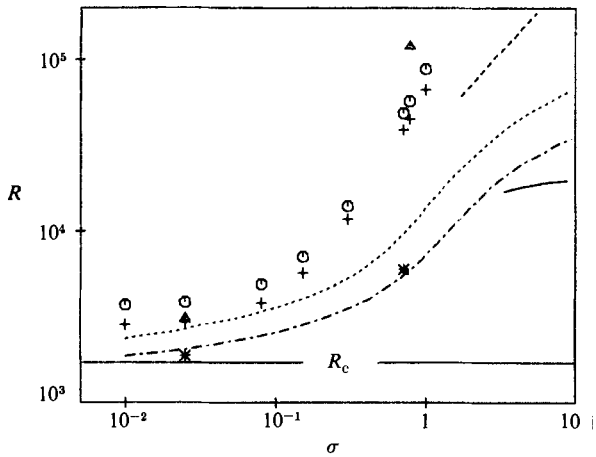

FIGURE 7. Rayleigh number R versus Prandtl number σ for several transitions. We have plotted the results for the critical wavenumber $a = 3.117$, not for the wavenumber corresponding to the minimum R-value. We display the values R_T(Ⓣ), R_n(+), and R_t(△) together with the bifurcation to the oscillatory instability R_{osc}(*) found by Clever & Busse (1974). Dotted and dashed lines correspond to different transitions found experimentally – see Krishnamurti (1973) figure 4. R_c means critical Rayleigh number.

bifurcations appear to be one-sided, but they are not. The emergent branch does not cross the bifurcation point, for it doubles back. This is a consequence of the $\xi \to -\xi$ symmetry discussed in §2.3 for there is no difference between the Nusselt numbers associated with each family of solutions.

In figure 6 we have plotted the Rayleigh numbers R_T and R_n for the case of mercury, together with Clever & Busse's (1974) results for the oscillatory instability and Krishnamurti's (1973) measurements for the first and second transitions to time dependence. The minimum of both Rayleigh numbers is for R_n and it is shown to be

at $R = 2650$, $a = 2.8$, in between the transitions at $R_1 = 2400$ and $R_2 = 3150$ reported by Krishnamurti. In figure 7 we have shown the same Rayleigh numbers R_T and R_n as in the previous figure but this time for the critical wavenumber a_c, and plotted versus the Prandtl number. We have chosen as a frame a section of Krishnamurti's (1973) figure 4, placing our results on top of it. We should realize in looking at this figure that the Rayleigh numbers displayed for the transitions do not correspond to their minimum values. Therefore, the agreement is fairly good for low-Prandtl-number fluids and discrepancies increase with σ. The transitions we have found for liquid helium and air are much too distant from any of the reported transitions to trust the model there. For the record, we report the values $R_T = 57377$ and $R_n = 45134$ for $\sigma = 0.78$.

4.1. *Stability of steady solutions*

The next step is to examine the stability of the steady solutions. Thus, we have carried out a linear stability analysis of system (2.19) in the neighbourhood of a $\xi \neq 0$ steady solution. Consistent with our purposes, we have perturbed this system, keeping for parameters a and C the same values in the perturbed equations as in the unperturbed ones.

The spectrum of the linear operator cannot be easily classified, since real and complex eigenvalues are mixed in some regions of parameter space. Therefore, we have followed a standard procedure in order to solve the problem – eigenvalues and eigenfunctions have been split into their real and imaginary parts, with the whole system being reduced to a real-valued ordinary differential equation of order twenty. The system is too lengthy to be displayed here. It can be found in Mercader (1985). The numerical results have been obtained by using the BODEL macrocompiler developed by E. Graham, which solves a system of first-order ordinary differential equations using second-order-accurate finite-difference schemes. The resulting eigenvalue problem is treated as a nonlinear algebraic system with the unknowns being both the eigenvalue and the eigenvector, and the system is solved iteratively by using a Newton–Raphson technique. The number of mesh points taken was 101, though only a few eigenvalues and eigenvectors were computed for each set of parameters.

The stability problem has been worked on for mercury and liquid helium and the results have been included in figures 4 and 5. There we show the three points: R_T, R_n and R_t; from the first bifurcation point R_T there emerge two unstable branches, with the spectrum for the new branch being a mixture of real and complex eigenvalues. At nose point R_n there is a change in stability and each solution becomes stable. Again, at value R_t, there is a bifurcation, this time with a complex eigenvalue crossing the imaginary axis. This is a Hopf bifurcation with angular frequencies $\omega = 0.55$ at $R_t = 3117$ for mercury, and $\omega = 130$ at $R_t = 1.2 \times 10^5$ for liquid helium. The corresponding periods in thermal units, $t = 2\pi/\omega$, are $t = 11.4$ and $t = 0.048$, respectively. In a search for completeness, we have included R_T in figure 7 discussed above.

5. Time-dependent solutions

System (2.19) has been time marched in the range of parameters where the analysis of stability made in the previous section announces the existence of non-steady solutions. Since we have concentrated on low-Prandtl-number fluids we can expect, from inspection, the presence of two timescales. In order to elucidate this point, we

have rescaled the variables as $\tilde{W} = W/\sigma$, $\tilde{\xi} = \xi/\sigma$, $\tilde{\theta} = \theta/\sigma$ on the assumption that the Reynolds number stays near its critical value. For consistency with the scaling we must also change the timescale from thermal to viscous as $\partial_\tau = \sigma^{-1}\partial_t$. Equation (2.7) can now be written at leading order in σ as

$$(\partial_\tau - \nabla^2)\nabla^2\tilde{W} = -Ra^2\tilde{\theta} + C[\tilde{W}\nabla^2\partial_z\tilde{W} + 2\,\partial_z\tilde{W}\nabla^2\tilde{W} + 3\tilde{\xi}\partial_z\tilde{\xi}], \tag{5.1a}$$

$$(\partial_\tau - \nabla^2)\tilde{\xi} = C[\tilde{\xi}\partial_z\tilde{W} - \tilde{W}\partial_z\xi], \tag{5.1b}$$

$$0 = \tilde{W} + \nabla^2\tilde{\theta}, \tag{5.1c}$$

where (2.19*d*) has been integrated at leading order to $\partial_z\bar{T} = -1$. This zero-order limit remains valid while both the variables and the ∂_τ-derivatives remain of order one. When either or both of these conditions break down, (5.1) becomes a singular limit of (2.7), thus entering the fast limit. The fast limit of (2.7) can be easily obtained by assuming the variables W, ξ and θ to be order one and again taking the thermal timescale $\partial_t = O(1)$ for the time derivatives. At leading order in σ the new system is identical with (2.19) but without the source term $Ra^2\theta$ and, eventually, without the boundary-layer terms $\sigma\nabla^2$ in (2.19*a*, *b*). Therefore, we must expect the system to collapse towards the null solution but, this state being unstable for the full system, the amplitudes must increase and the slow limit (5.1) is again reached. This is a plausible result and is confirmed by our numerical results, so we have avoided the awkward problem of doing an asymptotic expansion with boundary layers in both space and time. We may then expect two different types of solution:

(i) the Reynolds number of the primary flow stays close to its critical value for the onset of oscillations and (5.1) remains valid throughout the time period;

(ii) the Reynolds number grows at values that are larger than critical, and the system enters a limit cycle.

Both types of solution can be easily identified. In the former the condition $\partial_z\bar{T} = -1$, implicit in (5.1), implies a small convective transport throughout the time period (i.e. $N-1 \approx 0$), while in the latter we can expect large oscillations in flux.

5.1. *The numerical scheme*

System (2.19) has been broken down into a set of first-order partial differential equations as

$$\left.\begin{aligned} \partial_t X_i &= A_{ij}\partial_z X_j + F_i(X_1 \ldots X_N), \\ 0 &= B_{jl}\partial_z X_l + C_{jl}X_l, \end{aligned}\right\} \quad i = (1, \ldots, k); \quad j = (k+1, \ldots, N); \quad l = (1, \ldots N),$$

where $\{A_{ij}\}$, $\{B_{jl}\}$ and $\{C_{jl}\}$ are constant matrices, $k = 4$ and $N = 10$. Writing a system of partial differential equations as formed by equations with and without time derivatives is a formal way of treating each equation with an identical numerical scheme. The preference for breaking the system down into first-order instead of second-order equations has been dictated by the simplicity of the use of the BODEL macrocompiler developed by E. Graham. This is a code that generates a box-type implicit scheme – see, for instance, Telionis (1981) and references therein. Time and space derivatives – all of which are first order – are computed as a function of four grid points on the mesh, as

$$[\partial_t X]_{ij} = \frac{X_{i,j+1} + X_{i+1,j+1} - X_{i,j} - X_{i+1,j}}{2\Delta t},$$

$$[\partial_z X]_{ij} = \frac{X_{i+1,j+1} - X_{i,j+1}}{\Delta z},$$

where subindices i and j stand for space and time, respectively, in the usual way. Therefore, the scheme is implicit with spatial derivatives in each mesh being centred in space but advanced in time. Time derivatives are centred in space and time. If, as usual, the diffusion equation is taken for a test, the scheme is found to be consistent and stable. It has been taken as advanced in time to prevent spurious oscillations, so we may expect any oscillation to be of physical origin and possibly slightly damped. This scheme has been proved to be remarkably stable but highly sensitive to the choice of the time step, partly because of the stiffness of the system. In fact, the most important problem has arisen from the existence of nearby solutions, with the system jumping from one to the next or, even, from the proximity of a homoclinical orbit. The problem has always been solved by reducing the time step. It is important to report here that sometimes a reduction in time step forced a spurious periodic orbit to collapse towards a steady solution.

As criteria for choosing the number of mesh points and the time interval we have used the errors in the periods. We have assumed that the choice was correct if by halving the time step or the mesh interval the period was not changed by more than a few percent, though in the more stiff systems we have been stricter. As an additional test, we have checked the nonlinear frequencies of periodic orbits emerging from a Hopf bifurcation against the linear frequencies, the latter computed using a different code and a different technique (see the previous section). The number of mesh points required proved not to be crucial in the domain explored, and it has been taken to be 51. On the other hand, the time interval was found to be critical. As a rule of thumb, we needed two or three hundred steps per period but, in some cases, more than two thousand were required. The CPU time for each step ranged from 10–20 s on a Vax-750.

5.2. *Results*

System (2.19) has been time marched in those regions where no steady solution has been found to be stable or where finite-amplitude instabilities could be expected. The location of these regions can be easily inferred from figures 4 and 5.

Convection in mercury

A conspicuous example of the solutions computed is the case $R = 3550$, $\sigma = 0.025$, $a = 3.117$ shown in figure 8. Here we have plotted their time sequences for the Reynolds numbers $Re = CW/\sigma$ and $Re_v = C\xi/\sigma$ evaluated at the centre of the layer ($z = 0.5$) together with the Nusselt number at the top N_T. In order to help with the presentation we have not plotted the transients, and the periodic oscillations have been cloned artificially several times. The solution displayed is a prototype of what we have called type (ii) above. Here it is very easy to identify the two timescales discussed above. A full period takes $t = 136.8$ thermal time units, half that time being devoted to an exponential growth of ξ, whose value changes by a factor of four while W remains almost constant – the amplitude of W only changes by 20%. Suddenly the amplitudes for W and ξ fall, taking a few thermal units for the whole excursion and the cycle starts again, this time with the sign of W reversed. Thus, we can idealize the cycle as follows: W takes its steady value for a few viscous time units ($\tau = 1.7$) with ξ growing exponentially as it corresponds to W being linearly unstable. In this way the primary flow becomes severely distorted and W decays towards the null solution in a few thermal units because $W$and θ are brought out of phase and the source term $\langle v_z T' \rangle$ decays to zero. Since the null solution is unstable, the fields are forced to grow again. This time they grow towards their mirror-symmetrical

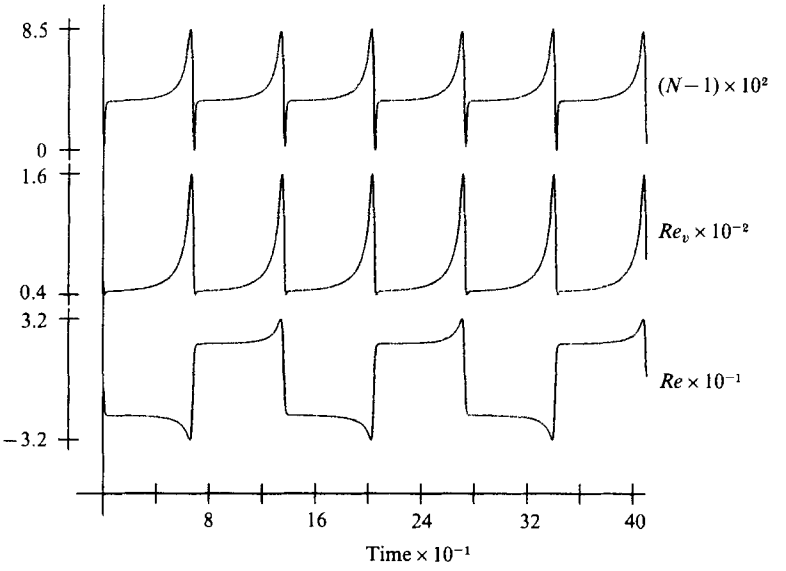

FIGURE 8. Time sequences corresponding to the case $R = 3550$, $\sigma = 0.025$, $a = 3.117$ for the magnitudes $Re = CW/\sigma$ and $Re_v = C\xi/\sigma$ evaluated at $z = 0.5$. N is the Nusselt number evaluated at the top layer $z = 1$. We have not displayed the Nusselt number at the bottom layer $z = 0$, because it shows an identical time sequence to N but shifted half a period. The period is $t = 136.8$ in thermal units and the mean flux is $N = 1.04$.

solution – see §2.4 – and the second half-cycle starts again. This jumping from one solution to the mirror-symmetrical one explains why the values for W and ξ at $z = 0.5$ cannot change in magnitude, even if W changes sign as shown by Re and Re_v in figure 8. It also explains the result, not displayed in the figure, that the time dependence for the Nusselt numbers on the top N_T and bottom N_B is exactly equal, although shifted half a period: the roles of $z = 0$ and $z = 1$ are exchanged once each half-period each time the fields jump from one solution to their mirror-symmetrical one. Such cyclical behaviour reminds us of an experiment described by Fauve *et al.* (1984*b*) for convection in mercury. Their container was cylindrical and the aspect ratio intermediate ($\Gamma = 3$). The rolls – three in number – were aligned by a magnetic field and the pictures – see their figure 3 – show a periodic rotation of the rolls around the vertical axis, always in the same direction, with a subsequent disruption of the whole structure. Next, the rolls were rebuilt with a reversed velocity and the cycle started again. We understand these rotations as a periodic growing of the vertical vorticity of the flow in the same way as happens in our case.

The solution presented above is a very peculiar example of a family of *full-cycle* solutions, 'full' meaning that W makes a full excursion from positive to negative values. A more genuine example of this family of solutions has been displayed in figure 9. It corresponds to $R = 6000$, other parameters being kept at the same values as in the previous case. The two-time structure is now less clear, but the stiffness of the system is still apparent and is reflected in the sensitivity of the frequencies to the time step. In order to compute this solution, 500 steps per period were necessary as a minimum requirement for a 1 % accuracy in the period, to be compared with 2500 steps for the $R = 3550$ case. The curves are now smoother and the time dependence for the Nusselt number is clearly different in the two half-periods. As the solution jumps in each period from one steady solution to its mirror-symmetrical one, the

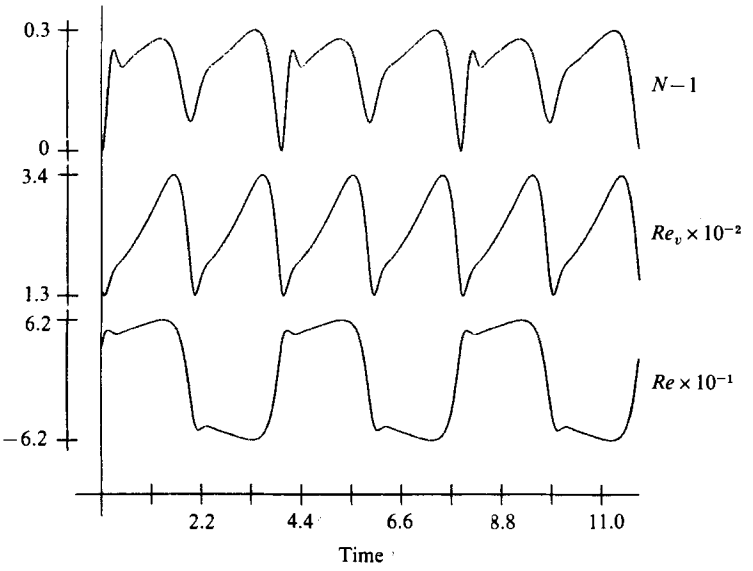

FIGURE 9. As figure 8, but for the case $R = 6000$, $\sigma = 0.025$, $a = 3.117$. The period is $t = 3.95$ and the Nusselt number $N = 1.21$.

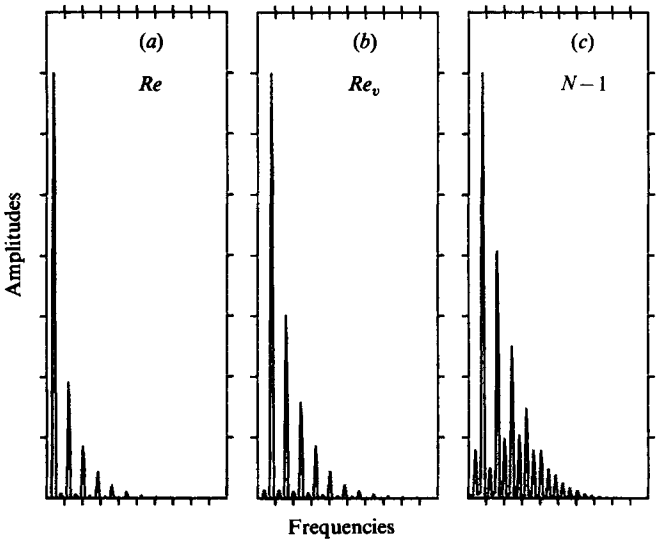

FIGURE 10. Fourier spectra for the time sequences displayed in figure 9 without the continuous component. The spectra for Re and Re_v show only odd or even components, respectively, and other components are negligible. Both components are mixed in the spectrum for N, giving rise to a double sequence characteristic of subharmonic bifurcations.

differences between both half-periods reflect the spatial asymmetry of these steady solutions. One of the most persistent signatures of this family of solutions is that W shows a period double that of ξ. This result can be seen clearly in the spectra shown in figure 10, where we have plotted Fourier spectra for W, ξ and N, in which, seeking for simplicity, we have not included the continuum component. The first two variables show monotonically decreasing sequences, respectively, of odd and even

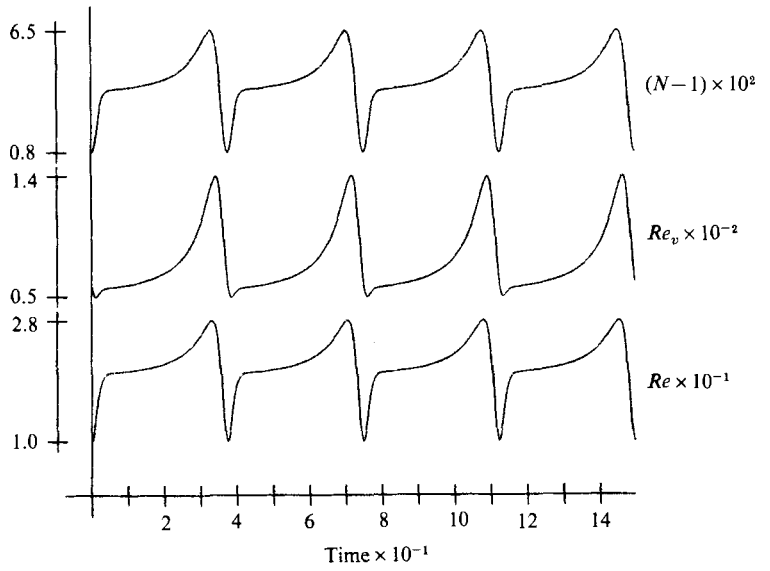

FIGURE 11. As figure 8 for the case $R = 3290$, $\sigma = 0.025$, $a = 3.117$. The period is $t = 38.5$ and $N = 1.04$. Notice that the periods are equal for all the variables.

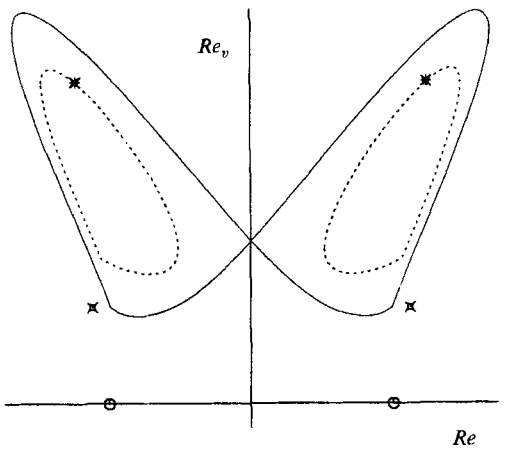

FIGURE 12. Upper half of an Re versus Re_v phase – map projection for the sequences displayed in figures 8 and 11 – solid and dot-dashed lines, respectively. The orbits correspond to the $z = 0.5$ value for Re and Re_v. The presence of a saddle point produces an abrupt change in the direction of the trajectories at the lower right and left corners of both orbits. Every solution computed in the range of Rayleigh- number values between to these two orbits decayed towards a $\xi = 0$ steady solution. We have also included in the figure the three steady solutions corresponding to the Rayleigh number of the solid-line orbit: saddle points ($\times$), stable nodal points ($\bigcirc$) and unstable foci($*$).

components, both signals being mixed in the Nusselt number where they give rise to a composite signal. In figure 10 (*c*) we have displayed the spectrum for N_T showing this double-sequence spectrum. At first sight figure 10(*c*) suggests a subharmonic bifurcation, but this might not be the case since odd components continuously grow from the birth of the full-cycle family of solutions. The first full-cycle solution has been found at $R = 3550$, between R_n and R_T, and the family survived until $R = 5 \times 10^4$, the maximum value of the Rayleigh number explored.

The full-cycle family of solutions does not emerge from the Hopf bifurcation shown in §4.1. This bifurcation has been found at $R_t = 3117$ and no solution of the present type emerged there. In figure 11 we have plotted the solution obtained at $R = 3290$, corresponding to the family that we have obtained at the bifurcation. It is clearly of type (i) (see definition above) as the Nusselt number remains very close to one and Re does not change sign with each cycle. We shall call them *half-cycle* solutions, as they do not jump from a steady solution to its mirror-symmetrical one. The clearest signature for these solutions is that W, ξ and N_T oscillate with the same frequencies and phases. The whole family dies out near $R = 3300$, where the system is attracted towards a $\xi = 0$ steady stable solution. In order to understand this behaviour we must recall that the half-cycle orbits emerge from a bifurcation on a branch $\xi \neq 0$, while $\xi = 0$ solutions are still stable, as can be seen in figure 4. Hence, if the trajectories come close enough to the stable, steady solution, the system enters a homoclinical orbit and the representative point is channelled towards the steady stable solution.

The proximity of a saddle point can be appreciated from figure 12, where we have superimposed two Re versus Re_v projections of the phase map corresponding to the solutions $R = 3290$ and $R = 3550$, whose time sequences have been plotted in figures 11 and 8, in which, seeking for simplicity, we show only the upper half of the map, the lower one being symmetrical. Both periodic orbits present an abrupt change in the directions of their trajectories, presumably induced by the proximity of the steady solution, as can be seen in the figure. In addition, each solution computed in the range of Rayleigh values delimited by the cases displayed in the figure has been attracted by the saddle point and caught by the steady stable solution. No periodic orbit has been found in this range of parameters. Whenever our code produced a periodic solution in this range, which happened very often, by halving the time step we get the orbit attracted towards the $\xi = 0$ steady solution. Thus, it seems that the transition between half-cycle and full-cycle solutions runs through some steady states and emerges as a reconnection of two half-cycle orbits into a full-cycle one. How they proceed is not clear to us, but whatever else it may be, this family of periodic solutions emerges with a finite amplitude. We now bring the reader's attention to the results on thermohaline convection by Huppert & Moore (1976), as they found a similar behaviour. Their periodic solutions show a spectrum like the one shown in figure 10, next to a gap with no periodic solutions. In their case, some aperiodic solutions were present in the neighbourhood.

In figure 13 we have plotted the frequencies obtained for periodic orbits as a function of the Rayleigh number. In a search for completeness we have also included the frequencies from the linear stability problem examined in §4. From this figure, together with figure 4, we get the following summary for convection in mercury:

(i) In the range $R_c < R < R_n$, with $R_n = 2940$, there exists only one (non-trivial) solution. It is steady, stable and $\xi = 0$.

(ii) In $2940 < R < R_t$, with $R_t = 3117$, there exist three steady solutions. Two of these are stable, one $\xi = 0$ and the other $\xi \neq 0$, the third one with $\xi \neq 0$ being unstable.

(iii) At $R_t = 3117$ the system shows a Hopf bifurcation. In the $R_t < R < 3300$ range we have found three steady solutions plus one half-cycle periodic solution. Only one of the steady solutions is stable – that with $\xi = 0$. As for the periodic orbit, it can be seen in figure 13 that the frequencies in the linear problem increase with R while the frequencies in the periodic motions decrease as the orbit is attracted by the steady solution.

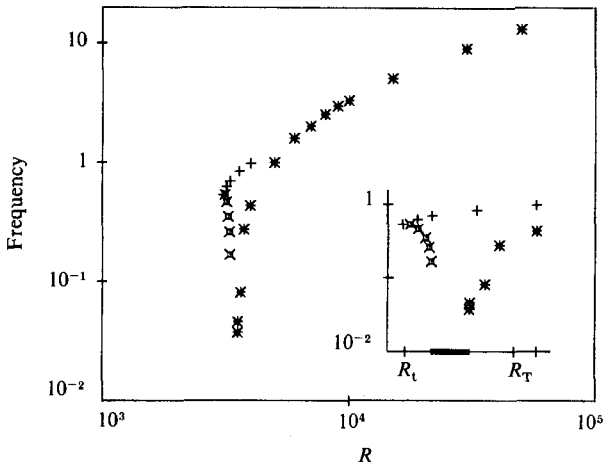

FIGURE 13. Frequencies versus Rayleigh number for $\sigma = 0.025$, $a = 3.117$ and two different families of solutions, half-cycle ($\times$) and full-cycle ($*$), together with the angular frequencies of the linear eigenvalue problem ($+$). In the lower right corner we have enlarged a section of the figure delimited by $R = 3000$ to 4000. The Rayleigh-number values have now been plotted on a linear scale instead of the log plot for the main figure. The frequency axis is logarithmic in both cases, now magnified. A double line in the enlarged Rayleigh axis delimits the range $3300 < R < 3550$ where we have not found any periodic solution. The symbols R_t, R_T are defined in the text.

(iv) In the $3300 < R < 3550$ range there exist three steady solutions, but only one of these is stable – that with $\xi = 0$. No periodic solution could be found in this range.

(v) At $R = 3550$ we have found the first full-cycle solution. It is born with finite amplitude and it is not clear if it is associated with any bifurcation – for instance, as a reconnection of two half-cycle unstable solutions. In the $3550 < R < R_T$ range, with $R_T = 3848$, the situation is similar to that in (iii) but now the periodic solution is full-cycle. At $R = R_T$ there is the bifurcation described in section 3.1.

(vi) In the $3848 < R$ range we have found only two unstable steady solutions plus one full-cycle solution. The limit of our exploration was $R = 5 \times 10^4$.

We have compared the frequencies obtained for our solutions with Krishnamurti's (1973) measurements in the $R = 2400$ to 3600 range. There are several points of coincidence. First, the periods she measured are in the range $t = 100$, $t = 60$, in thermal units. This is consistent with the value for our maximum period $t = 136.8$ for $R = 3550$ if we agree that in measuring the periods for the Nusselt number she measured the periods for the first overtone, not for the fundamental one, as suggested by figures 8 and 9. Secondly, she found that at $R = 3150$ the spectrum suddenly became much broader, showing a large number of higher frequencies, from which she could discriminate from the noise components ranging between the periods of $t = 100$ and $t = 1$. This is consistent with our results, as the time sequences we have obtained at $R = 3550$ show a very broad spectrum, its amplitudes decaying very slowly with increasing frequencies, in clear contrast with the spectra that we have obtained for smaller Rayleigh values.

As a final step we have examined the efficiency of the heat transport and in figure 14 we have plotted the time average of the Nusselt number in the periodic regime as a function of the Rayleigh number. For comparison we have included the Nusselt number for the steady branch displayed in figure 4, along with experimental results from Rossby (1969) and Krishnamurti (1973). For this figure we have used a

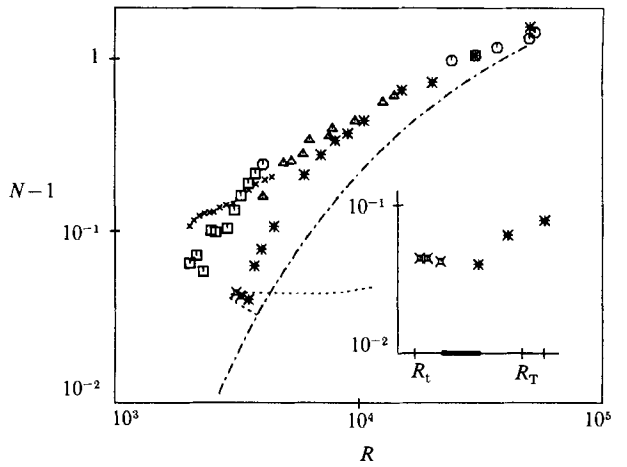

FIGURE 14. Nusselt number versus Rayleigh number for $\sigma = 0.025$, $a = 3.117$. The same symbols as in figure 13. We have included experimental results from Krishnamurti (1973) (×) and from Rossby (1969) (□, △, ○), the latter ordered as a sequence of decreasing aspect ratios. The dotted and dot-dashed lines are the solid lines of figure 4 in a log–log plot. We have enlarged a section of the figure in the lower right corner using the same criteria as in figure 13.

logarithmic scale for fluxes in order to magnify the differences between theory and experiments as they involve very small Nusselt numbers. It comes as a surprise to realize that the time-dependent regime is far more efficient in transporting heat than the steady one. This result is a consequence of both W and θ showing the appropriate phasing in their oscillations. As can be seen, the agreement between theory and experiment is almost perfect for intermediate Rayleigh numbers $R > 10^4$ and differences mostly involve Rayleigh numbers in the metastable region. Nevertheless, we must observe that the largest Nusselt values correspond to experiments with intermediate-aspect-ratio boxes, and the smallest ones to larger boxes. So, it might be that the agreement or disagreement has to be associated with the aspect ratio of the box, not with the range of Rayleigh numbers, but the question cannot yet be answered. Also, we can appreciate from the figure that the averaged flux decreases with R for the half-cycle solutions. We have no explanation for such an unexpected result, but we suggest a look at the three leftmost squares plotted in figure 14. Do they represent a subcritical branch or do they show a decrease in flux followed by a sudden jump, as is the case in the present results?

Convection in liquid helium and air

As pointed out before, in the cases of liquid helium and air the bifurcations take place at Rayleigh values where no transitions have been reported or where they are expected to be masked by previous bifurcations. However, they are illustrative of the behaviour of the system because, in contrast to the case of mercury, the transition from half-cycle solutions to full-cycle solutions does not take place in the presence of a steady attractor. Half- and full-cycle solutions show similar behaviour in helium to that in mercury. The half-cycle family bifurcates at $R_t = 1.2 \times 10^5$ from a standard Hopf bifurcation. We have not plotted any set of time sequences for these solutions as they look very similar to the ones shown for mercury. The new factor is the presence of a new family of solutions which we shall call *double-loop* because of their shape in the phase map. One of these solutions, corresponding to $R = 2 \times 10^5$, has

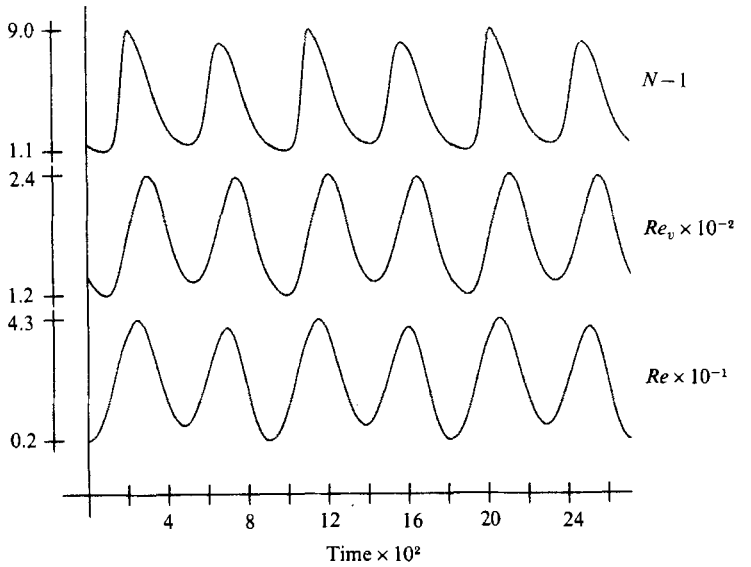

FIGURE 15. As figure 8 but showing double-loop solution at $R = 2 \times 10^5$, $\sigma = 0.78$, $a = 3.117$. The period is $T = 0.089$ and the mean Nusselt number $N = 5.07$. As in figure 11, every variable shows the same period.

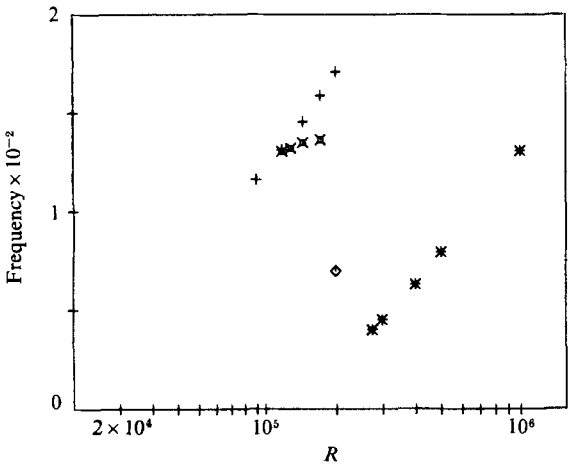

FIGURE 16. Frequencies versus Rayleigh number for $\sigma = 0.78$, $a = 3.117$. Symbols are the same as in figure 13 with the inclusion of (◇) for a double-loop solution. Frequencies jump discontinuously from $\omega = 136$ to $\omega = 69.8$ and $\omega = 40$.

been displayed in figure 15. It looks like the first stage in a subharmonic bifurcation with period being doubled. However, we should mention that the periodicity of this solution could be questioned as it takes a long time to enter a periodic orbit and we have not halved steps enough times to be completely confident. Since we had taken more than 3000 steps per period, we stopped halving because, in our opinion, we were close to using the brute-force method.

In figure 16 we have plotted the frequencies as a function of the Rayleigh number. Linear and nonlinear frequencies are coincident at the bifurcation, as expected, and they both increase with Rayleigh-number values, thus making a clear difference to

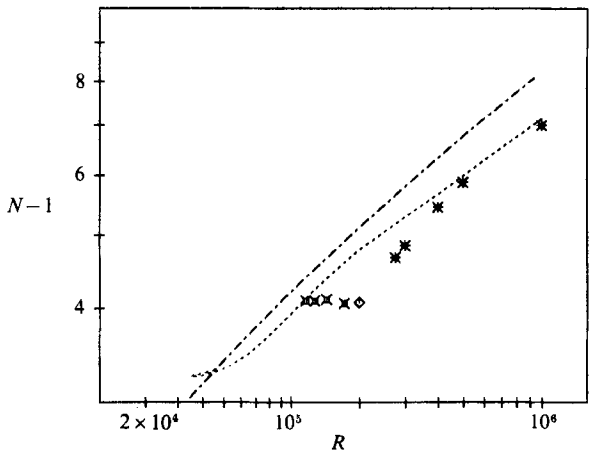

FIGURE 17. Nusselt number versus Rayleigh number for $\sigma = 0.78$, $a = 3.117$. The same symbols as in figure 16. The dotted and dot-dashed lines correspond to the solid lines in figure 5. The presence of two different laws (slopes N versus R), corresponding to two different families of solutions, can be noticed in the figure.

the case of mercury. Suddenly, these half-cycle solutions jump to a double-loop solution – we have computed only one example – with frequencies being halved. Frequencies then jump again, this time to a full-cycle solution. This jumping looks clearly like a subharmonic bifurcation since frequencies are halved each time and this might be taken as an indication of chaotic behaviour (Gollub 1980). However, our code was not well suited to a search for quasi-periodic or chaotic solutions and no systematic exploration has yet been done.

Finally, in figure 17 we have plotted the time-averaged Nusselt numbers as a function of Rayleigh number. There is a significant difference with respect to the case of mercury. Nusselt numbers are now smaller for the time-dependent regime than for the steady solution. Also, if these results were to be compared with experimental work, we would observe that the change from one family of solutions to the next takes place through a change in the slope of the N versus R curve. Changes in slope have been conjectured by some experimentalists as being associated with different families of solutions – see for instance Krishnamurti (1973) – and this conjecture seems to be consistent with the present results. As in the case of mercury – see figure 15 – Nusselt number decreases with Rayleigh number for half-cycle solutions, though now very slowly.

6. Conclusions

The present work has to be understood as a first attempt to explore the physics of non-straight structures in the low-Prandtl-number limit, as well as the contribution to their dynamics from the vertical vorticity field. We have used a highly truncated modal approach with the choice of modes being devised in such a way that they could display instabilities associated with the curvature of the primary flow, with a minimum of effort. The price paid for this simplicity is the absence of what we have called above 'shape instabilities', with the so-called oscillatory instability being the most relevant example of these in low-Prandtl-number fluids. Even if they are missing, however, the model reproduces with reasonable accuracy the time dependence observed in experiments on mercury. Frequencies and fluxes computed

for mildly supercritical Rayleigh numbers are consistent with experiments, mostly with experiments concerning containers of intermediate aspect ratio.

The agreement between our results and some experimental measurements might be confusing for we are assuming hexagonal planforms to model some experiments which definitely do not show such a geometry. There is, in our opinion, only one explanation: system (2.19) includes most of the modal components active in these contexts. For instance, in the Appendix we show that such a planform includes some signature of roll bending. However, such mathematical reasoning may make some readers uneasy. Therefore, we shall discuss a physical model borrowed from vorticity dynamics – see Leonard (1985) for a review. Leonard built a bend filament from the superposition of two vortices, one being straight and the other toroidal – D-shaped to be precise. They both shared the straight section of the D, with circulations chosen so as to cancel there. As a result, some axial flow was forced, with the D-shaped component providing all the forcing.

If these results can be extrapolated to the present context, we propose that any bent roll can be split up into two kinds of modes – say Fourier components – some of them cooperating to build straight rolls, others building toroidal flows. If so, our results are consistent with situations where the latter, but not the former, are destabilized. If the previous conjecture is added to Jones & Moore's (1979) results for axisymmetrical convection not showing any oscillatory instability in low-Prandtl-number fluids, we get the following picture: if the rolls show some bending, then the oscillatory instability can be inhibited, but an axial flow can be destabilized by the swirl. This might explain why our results are consistent with experiments for convection in mercury but not in liquid helium or air, for the oscillatory instability must be present in the latter, but not in the former. However, if convection is confined in tall cylinders (Mitchell & Quinn 1966), where the oscillatory instability is expected to be inhibited, numerical and experimental results agree even for air (Massaguer, Mercader & Blazquez 1987).

Cross's (1982) results are encouraging, for he was able to isolate some sources of instability as being associated with roll bending. Even if the physics of the instability is different, it is relevant, for he found one such source near the boundaries, induced by the bending of the roll axis. This could explain why our results show the best agreement with convection if the container aspect ratio is intermediate, as can be seen from figure 14. If the aspect ratio of the container is large, the agreement is not so satisfactory, but there are still some clear signatures of swirl instability, suggesting that, besides the geometry, roll bending may be forced by the initial conditions or even dynamically forced if some shape instability is active.

It is also noteworthy that a continuous exchange of kinetic energy between the vertical components of vorticity and velocity could result in an enhancement of the heat transport, as is the case for mercury. The only reason for this increased efficiency comes from the temporal coherence between velocity and temperature, a situation that can be understood as a consequence of the large ratio between the two time-scales characteristic of the fluid. All variables must enter the fast section of the cycle at the same time. Thus, rather than any variable choosing its phases more or less randomly, it must choose them in such a way that its lag is not larger than the faster of both time-scales of the cycle. Thus, low-Prandtl-number convection is a beautiful example of coherence in both time and space.

The model that we have explored is also a promising one as there are some signatures of subharmonic bifurcations in regions where experiments give hints of chaotic behaviour. These regions in parameter space deserve more work, and we may

speculate about how many of these signatures will survive once the model is improved with the inclusion of new modes. The answer is not obvious, but we are fairly confident, since the solutions found display large amplitudes and a reasonable consistency with experimental results.

During the course of present work we have enjoyed profitable discussions with Drs A. Falques, S. Fauve, R. Krishnamurti, F. Marques, J. Toomre, J. E. Wesfreid and J. P. Zahn. Our warmest thanks are due to all of them. Thanks are due also to Dr E. Graham whose BODEL code has been used for part of the present computations. Criticism from the referees has been of great assistance in improving the manuscript, our thanks going to them. The present work has been supported by the Comisión Asesora de Investigación Científica y Técnica, Spain.

Appendix. Two-dimensional flows with swirl

In this Appendix we examine the energy sources for instabilities associated with a non-zero vertical vorticity component. As a first step, if (2.3) is multiplied by ϕ and integrated over the whole volume, by using the definition (2.2a) and integrating by parts, we obtain the balance equation

$$\sigma^{-1}\partial_t\langle\tfrac{1}{2}v_{\mathrm{P}}^2\rangle+\langle|\boldsymbol{\nabla}\boldsymbol{v}_{\mathrm{P}}|^2\rangle = R\langle v_z T'\rangle-\sigma^{-1}\langle\boldsymbol{v}_{\mathrm{P}}\cdot(\boldsymbol{v}\cdot\boldsymbol{\nabla}\boldsymbol{v})\rangle, \tag{A 1}$$

where the angle brackets designate a volume average and the velocity has been split up as $\boldsymbol{v}=\boldsymbol{v}_{\mathrm{P}}+\boldsymbol{v}_{\mathrm{T}}$, and where $\boldsymbol{v}_{\mathrm{P}}=\boldsymbol{\nabla}\times\boldsymbol{\nabla}\times(\phi\boldsymbol{k})$ and $\boldsymbol{v}_{\mathrm{T}}=\boldsymbol{\nabla}\times(\psi\boldsymbol{k})$ are, respectively, the poloidal and toroidal components of the velocity field. Also, the volume average of (2.4) times ψ can written as

$$\sigma^{-1}\partial_t\langle\tfrac{1}{2}v_{\mathrm{T}}^2\rangle+\langle|\boldsymbol{\nabla}\boldsymbol{v}_{\mathrm{T}}|^2\rangle = -\sigma^{-1}\langle\boldsymbol{v}_{\mathrm{T}}\cdot(\boldsymbol{v}\cdot\boldsymbol{\nabla}\boldsymbol{v})\rangle. \tag{A 2}$$

By adding (A 1) and (A 2) we obtain the well-known energy balance

$$\sigma^{-1}\partial_t\langle\tfrac{1}{2}v^2\rangle+\langle|\boldsymbol{\nabla}\boldsymbol{v}|^2\rangle = R\langle v_z T'\rangle \tag{A 3}$$

where the relationships $\langle\boldsymbol{v}_{\mathrm{T}}\cdot\boldsymbol{v}_{\mathrm{P}}\rangle=0$ and $\langle\boldsymbol{v}\cdot(\boldsymbol{v}\cdot\boldsymbol{\nabla}\boldsymbol{v})\rangle=0$ have been used.

The splitting of (A 3) into its toroidal and poloidal parts shows the source of instability for the toroidal component to be in the right-hand side of (A 2). If, for any reason, this source term is zero, the solution is attracted towards a $\boldsymbol{v}_{\mathrm{T}}=0$ field and (A 1) can be reduced to (A 3) while (A 2) becomes identically zero. Moreover, $\boldsymbol{v}_{\mathrm{T}}=0$ identically satisfies (A 2) but not the vorticity equation (2.4), for then $\omega_z=0$ is not solution unless

$$\boldsymbol{\omega}_{\mathrm{P}}\cdot\boldsymbol{\nabla}v_z=0, \tag{A 4}$$

where now $\boldsymbol{\omega}_{\mathrm{P}}=\boldsymbol{\nabla}\times\boldsymbol{v}_{\mathrm{P}}$. What is left is a geometrical condition forcing the flow to be invariant along vorticity lines – horizontal by hypothesis. This condition can be written more explicity as

$$\frac{\partial(\nabla^2\phi,\nabla_1^2\phi)}{\partial(x,y)}=0.$$

Let us now consider a flow fulfilling condition (A 4). A first source of instabilities comes from perturbations violating this condition. We have called them *shape instabilities* – see (2.15) – but these are not the only possible instabilities. The flow can be unstable against vertical vorticity even if the perturbations fulfil condition (A 4). In order to examine this type of instability we must realize that an impor-

tant set of solutions to (A 4) is two-dimensional, in the sense that $\phi = \phi(\alpha, z)$ with $\alpha = \alpha(x, y)$. We shall concentrate on these.

We are now interested in building a family of two-dimensional flow with prescribed geometry. We shall proceed in the following way: given a bundle of horizontal lines $\beta = \beta(x, y)$, there always exists an orthogonal system of coordinates (α, β, z) with $\alpha = \alpha(x, y)$. By writing (2.2) in the new coordinate system, and taking $\partial_\beta = 0$ we obtain

$$\left.\begin{aligned} \boldsymbol{v}_{\mathrm{P}} &= \partial_{\alpha z}\phi\,\boldsymbol{e}_\alpha - \nabla_1^2\phi\,\boldsymbol{k}, \\ \boldsymbol{v}_{\mathrm{T}} &= -\partial_\alpha\psi\,\boldsymbol{e}_\beta, \\ \boldsymbol{\omega}_{\mathrm{P}} &= \partial_\alpha(\nabla^2\phi)\,\boldsymbol{e}_\beta, \\ \boldsymbol{\omega}_{\mathrm{T}} &= \partial_{\alpha z}\psi\,\boldsymbol{e}_\alpha - \nabla_1^2\psi\,\boldsymbol{k}, \end{aligned}\right\} \tag{A 5}$$

where $\boldsymbol{e}_\alpha$ and $\boldsymbol{e}_\beta$ are the natural vectors along the α- and β-coordinate directions. In the case where $\psi = 0$ the flow becomes a vorticity tube – i.e. a roll – along a β-line. Straight rolls, axisymmetrical tori and one-hexagon planforms are particular examples of these two-dimensional structures which we shall call simply *bent-rolls*.

Equation (A 5) indicates that even with $\partial_\beta = 0$ a toroidal component $\boldsymbol{v}_{\mathrm{T}}$ can be present. This component is called the *swirl* in vorticity dynamics and constitutes the main ingredient of the instability analysed. In order to understand where the energy for the swirl comes from we have to split up the energy source in (A 2) as

$$\langle \boldsymbol{v}_{\mathrm{T}}\cdot(\boldsymbol{v}\cdot\nabla\boldsymbol{v})\rangle = \langle \boldsymbol{v}_{\mathrm{T}}\cdot(\boldsymbol{v}_{\mathrm{P}}\cdot\nabla\boldsymbol{v}_{\mathrm{P}})\rangle + \langle \boldsymbol{v}_{\mathrm{T}}\cdot(\boldsymbol{v}_{\mathrm{T}}\cdot\nabla\boldsymbol{v}_{\mathrm{P}})\rangle,$$

where the conditions $\langle \boldsymbol{v}_{\mathrm{T}}\cdot(\boldsymbol{v}_{\mathrm{T}}\cdot\nabla\boldsymbol{v}_{\mathrm{T}})\rangle = 0$ and $\langle \boldsymbol{v}_{\mathrm{T}}\cdot(\boldsymbol{v}_{\mathrm{P}}\cdot\nabla\boldsymbol{v}_{\mathrm{T}})\rangle = 0$ have been used. Now, by using the well-known identity $\boldsymbol{v}\cdot\nabla\boldsymbol{v} = \boldsymbol{\omega}\times\boldsymbol{v} + \frac{1}{2}\nabla^2$ and integrating by parts we obtain

$$\langle \boldsymbol{v}_{\mathrm{T}}\cdot(\boldsymbol{v}_{\mathrm{P}}\cdot\nabla\boldsymbol{v}_{\mathrm{P}})\rangle = \langle \boldsymbol{v}_{\mathrm{T}}\cdot\boldsymbol{\omega}_{\mathrm{P}}\times\boldsymbol{v}_{\mathrm{P}}\rangle = 0$$

because $\boldsymbol{v}_{\mathrm{T}}$ and $\boldsymbol{\omega}_{\mathrm{P}}$ are parallel – see (A 5). Also

$$\langle \boldsymbol{v}_{\mathrm{T}}\cdot(\boldsymbol{v}_{\mathrm{T}}\cdot\nabla\boldsymbol{v}_{\mathrm{P}})\rangle = \langle v_{\mathrm{T}}^2\,\partial_{\alpha z}\phi\,K_\beta\rangle,$$

with K_β being the curvature of the β-line if β is the arc length. Therefore, the source term in (2.16) can be written explicitly for a two-dimensional flow as

$$\sigma^{-1}\partial_t\langle\tfrac{1}{2}v_{\mathrm{T}}^2\rangle + \langle|\nabla\boldsymbol{v}_{\mathrm{T}}|^2\rangle = -\sigma^{-1}\langle v_{\mathrm{T}}^2\,\partial_{\alpha z}\phi\,K_\beta\rangle, \tag{A 6}$$

showing that, as far as two-dimensional flows are concerned, only those structures curved along their longitudinal axis can generate a toroidal component. This situation is very similar to the possibility of axial velocity within the core of curved vortex filaments – see Widnall (1975) for a review on the subject. Clearly, the existence of an along-roll velocity componenent – i.e. axial flow – is not consistent with the condition $\partial_\beta = 0$ unless the roll forms a closed loop, otherwise it would imply a net mass flux in the β-direction. However, we can expect swirl even in open rolls if this constraint breaks down near the boundary and a boundary layer with $\partial_\beta \neq 0$ is formed, as might be the case for flows confined in finite boxes.

REFERENCES

Ahlers, G. & Behringer, R. P. 1978 *Phys. Rev. Lett.* **40**, 712.

Baker, L. & Spiegel, E. A. 1975 *J. Atmos. Sci.* **82**, 1909.

Behringer, R. P. & Ahlers, G. 1982 *J. Fluid. Mech.* **125**, 219.

Busse, F. H. 1972 *J. Fluid Mech.* **52**, 97.

Busse, F. H. 1978 *Rep. Prog. Phys.* **41**, 1929.

CLEVER, R. M. & BUSSE, F. H. 1974 *J. Fluid Mech.* **65**, 625.

COLES, D. 1965 *J. Fluid Mech.* **21**, 385.

CROSS, M. C. 1982 *Phys. Rev.* **25**, 1065.

FAUVE, S., LAROCHE, C., LIBCHABER, A. & PERRIN, B. 1984*a* *Phys. Rev.* **52**, 1774.

FAUVE, S., LAROCHE, C., LIBCHABER, A. & PERRIN, B. 1984*b* In *Cellular Structures in Instabilities.* (ed. J. E. Wesfreid and S. Zaleski). Lecture Notes in Physics, vol. 210, pp. 278–284. Springer.

GOLLUB, J. P. 1980 In *Systems far from Equilibrium* (ed. L. Garrido). Lecture Notes in Physics, vol. 132, pp. 162–180. Springer.

GOUGH, D. O., SPIEGEL, E. A. & TOOMRE, J. 1975 *J. Fluid Mech.* **68**, 695.

HUPPERT, H. E. & MOORE, D. R. 1976 *J. Fluid Mech.* **78**, 821.

JONES, C. A. & MOORE, D. R. 1979 *Geophys. Astrophys. Fluid Dyn.* **11**, 245.

JONES, C. A., MOORE, D. R. & WEISS, N. O. 1976 *J. Fluid. Mech.* **73**, 353.

KRISHNAMURTI, R. 1973 *J. Fluid Mech.* **60**, 285.

LEONARD, A. 1985 *Ann. Rev. Fluid Mech.* **17**, 523.

LIPPS, F. B. 1976 *J. Fluid Mech.* **75**, 113.

LOPEZ, J. M. & MURPHY, J. O. 1984 *Aust. J. Phys.* **37**, 531.

MALKUS, W. & VERONIS, G. 1958 *J. Fluid Mech.* **4**, 225.

MARCUS, P. S. 1981 *J. Fluid Mech.* **103**, 241.

MASSAGUER, J. M. & MERCADER, I. 1984 In *Cellular Structures in Instabilities* (ed. J. E. Wesfreid and S. Zaleski). Lecture Notes in Physics, vol. 210, pp. 270–277. Springer.

MASSAGUER, J. M., MERCADER, I. & BLAZQUEZ, S. 1987 In *Advances in Turbulence* (ed. G. Comte-Bellot & J. Mathieu), pp. 49–53. Springer.

MCLAUGHLIN, J. B. & ORZAG, S. A. 1982 *J. Fluid Mech.* **122**, 123.

MERCADER, I. 1985 Convección a paqueño número de Prandtl. Thesis, University of Barcelona.

MERCADER, I. & MASSAGUER, J. M. 1983 In *Proc. IV Asamblea Nacional de Astronomia y Astrofisica*, vol. 1, p. 455.

MITCHELL, W. T. & QUINN, J. A. 1966 *AIChE J.* **12**, 1116.

MURPHY, J. O. & LOPEZ, J. M. 1984 *Aust. J. Phys.* **37**, 179.

MURPHY, J. O. & LOPEZ, J. M. 1985 *Aust. J. Phys.* **38**, 41.

MURPHY, J. O. & YANNIOS, N. 1985 *Proc. Astron. Soc. Aust.* **6**, 216.

NEWELL, A. C. & WHITEHEAD, J. A. 1969 *J. Fluid Mech.* **38**, 27.

ROSSBY, H. T. 1969 *J. Fluid. Mech.* **36**, 309.

SCHLÜTER, A., LORTZ, D. & BUSSE, F. H. 1965 *J. Fluid Mech.* **23**, 129.

SIGGIA, E. D. & ZIPPELIUS, A. 1981 *Phys. Rev. Lett.* **47**, 835.

SULEM, P. L., SULEM, C. & THUAL, O. 1985 *Prog. Astron. Aeron.* **100**, 125.

TOOMRE, J., GOUGH, D. O. & SPIEGEL, E. A. 1977 *J. Fluid Mech.* **79**, 1.

TOOMRE, J., GOUGH, D. O. & SPIEGEL, E. A. 1982 *J. Fluid Mech.* **125**, 99.

TELIONIS, D. P. 1981 *Unsteady Viscous Flows*, p. 53. Springer.

VAN DER BORGHT, R. 1976 *Aust. J. Phys.* **29**, 305.

WALDEN, R. W. 1983 *Phys. Rev.* **A 27**, 1255.

WIDNALL, S. E. 1975 *Ann. Rev. Fluid Mech.* **7**, 141.